第 41 卷 第 1 期
2020 年 1 月
焊 接 学 报
TRANSACTIONS OF THE CHINA WELDING INSTITUTION
Vol. 41(1):44 − 49
January 2020

旋转电弧 GMAW 堆焊短路过渡熔池动态仿真

毛志伟[1]， 黄涛[1]， 周少玲[2]
(1. 南昌大学, 南昌, 330031; 2. 江西工业职业技术学院, 南昌, 330095)

摘要: 为探究旋转电弧 GMAW 堆焊短路过渡时熔池的温度和对流分布规律, 利用 Flow-3D 软件建立三维数学模型, 采用球形旋转热源模型, 考虑重力、熔滴拖拽力、表面张力、浮力作用, 模拟了堆焊状态下, 工件材料为 Q235 的旋转电弧 GMAW 短路过渡的熔池成形规律. 采用流体体积法追踪熔滴过渡和熔池表面的自由变形,并分析熔滴进入熔池时熔池内部温度场和流场的变化. 结果表明, 熔池形成过程中, 旋转熔滴对熔池有搅拌作用, 并使熔池内部液态金属活性增强, 流速变快, 熔池内部液态金属体积变大, 熔池的宽度变大. 模拟预测的焊缝尺寸、形状与试验吻合良好. 为优化焊接工艺参数、改善旋转电弧 GMAW 堆焊焊缝质量提供参考依据.

关键词: 旋转电弧焊; 球形旋转热源模型; 熔池流动; 熔池凝固
中图分类号: TG 444　　**文献标识码:** A　　**doi:** 10. 12073/j. hjxb. 20190528002

0 序言

熔化极气体保护焊 (gas metal arc welding, GMAW) 在焊接生产中有着广泛应用. 工件在电弧热和熔滴周期性冲击下, 熔化并形成熔池. 熔池内流体流动受到电弧压力、电磁力、重力、表面张力、浮力、熔滴冲击力等因素影响. 探究旋转电弧焊熔池成形时温度和对流分布规律, 对研究旋转电弧焊接过程电流信号变化规律、焊接成形质量等有着重要意义.

Wu 等人[1] 采用 Flow-3D 分析了不同焊接速度和送丝速率下的熔池行为, 结果表明焊接速度越快, 电弧就越不稳定, 在工件表面可能会产生咬边, 电导率的提高可增加电弧的稳定性, 并通过试验验证了仿真结果. Cho 等人[2] 采用 Flow-3D 模拟了各种焊接位置 V 形槽焊接过程, 因不同重力效应, 得到了不同的熔池流动模式、凝固时间、温度分布和焊缝形状. Wang 等人[3] 模拟了 GMAW 熔滴动态撞击熔池过程中, 熔滴撞击动量与表面张力等因素引起的熔池瞬态形状变形. Hozoorbakhsh 等人[4] 模拟了激光焊接参数对温度场以及熔池形成的影响, 预测了薄板不锈钢激光焊接焊缝的几何形状和凝固形态. Wu 等人[5-6] 采用高速摄影系统对熔池的瞬态图像进行了采集, 分析了熔池形成、对流和冲击的差异; 利用 Flow-3D 软件建立三维仿真模型, 模拟了 A36 船用低碳钢熔化极惰性气体保护焊的瞬态温度场和流场, 分析了起弧后熔池形成和熄弧后熔池凝固两个过程中熔滴冲击力、电磁力对液态金属流动影响. Cho 等人[7]基于三维数值传热理论建立了流体流动模型, 采用流体体积法分析了埋弧焊过程中液体流动和温度变化规律, 此外还分析了自由表面成形机理. Tong 等人[8] 对焊接过程中焊丝无摆动和 e 型摆动轨迹的熔池金属相变及元素分布进行了模拟, 得到了这两种运动方式下熔池成形特征. Desmaison 等人[9] 针对 18MND5 材料建立了激光-GMA 复合焊接模型, 并对该复合焊接过程进行模拟, 得到了熔池成形过程中流场和温度场分布. 张世亮等人[10] 采用 FLUENT 软件分析了不同条件下熔化极气体保护焊熔池动态行为, 结果表明熔池内流体流速相对于电弧等离子体流速较小, 电弧等离子体冲击熔池自由液面后, 迅速沿熔池自由液面向周边快速流动, 并对其产生切应力. Qiao 等人[11] 针对套管补口角焊缝, 通过拟合方法确定双椭球热源的参数, 模拟得到的熔池形态与实际焊缝吻合较好.

目前, 还未见有学者通过建立热源模型研究旋转电弧 GMAW 熔池的形成过程. 为研究旋转电弧

收稿日期: 2019 − 05 − 28
基金项目: 国家自然科学基金资助项目 (51265036)

GMAW 熔池成形过程, 以堆焊为例, 在分析影响熔池成形过程的主要因素基础上, 采用球形热源模型, 运用 Flow-3D 软件建立其三维数值模型, 研究主要影响因素动态作用下, 熔滴进入熔池时熔池内的金属流动状态.

1　旋转电弧堆焊物理模型

为对旋转电弧进行温度场与流场分析, 首先需建立其三维有限元数值模型. 依据旋转电弧 GMAW 堆焊工艺要求, 相关工艺参数如表 1 所示.

表 1　焊接试验参数

Table 1　Welding experiment parameters

焊件材料	焊接电压 U/V	焊接电流 I/A	焊接速度 v/(mm·s^{-1})	旋转频率 f/Hz	焊丝伸出长度 l/mm	旋转半径 r/mm	保护气流量 q/(L·min^{-1})	焊件初始温度 T/℃	保护气
Q235A	23	200	30	20	12	3	10	30	80%Ar + 20%CO_2

焊接试验方式为堆焊, 单道焊缝, 焊缝与母材的材料属性相同. 工件尺寸分别为 150 mm × 100 mm × 5 mm. 焊接物理模型如图 1 所示.

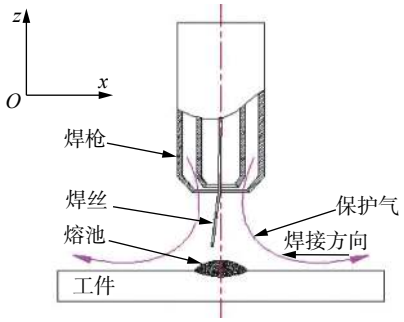

图 1　焊接物理模型

Fig. 1　Physical model of welding

为简化计算, 进行如下假设: ①热源为球形, 热源半径为定值, 从熔池上方固定位置滴入熔池, 熔滴的温度以及动能恒定; ②一个旋转周期内, 热源数量为 4 个, 短路过渡, 热源稳定连续进入熔池; ③仿真过程中的液态金属为牛顿流体, 其具有不可压缩以及稳定粘性, 液态金属之间流动状态为层流; ④焊接仿真过程中熔池表面的热流密度以及焊接过程中的电弧力都遵从高斯分布; ⑤液态金属的密度、粘度、热导率等热物理属性都随温度变化而变化.

2　控制方程

GMAW 焊熔池模拟采用三维笛卡尔坐标系, 运用 Flow-3D 求解包括质量守恒方程、动量守恒方程、能量守恒方程在内的控制方程, 并用流体体积法 (volume of fluid, VOF) 追踪熔滴过渡和熔池表面的自由变形.

2.1　物理控制方程

质量守恒方程

$$\frac{\partial u}{\partial r}+\frac{\partial v}{\partial z}+\frac{u}{r}=0 \tag{1}$$

动量守恒方程

$$\frac{\partial(\rho u)}{\partial t}+u\frac{\partial(\rho u)}{\partial r}+v\frac{\partial(\rho u)}{\partial z}= -\frac{\partial P}{\partial r}+u\left(\frac{\partial^2 u}{\partial r^2}+\frac{\partial^2 u}{\partial z^2}+\frac{\partial u}{r\cdot\partial r}-\frac{u}{r^2}\right)-J_z\cdot B_\theta \tag{2}$$

$$\frac{\partial \rho v}{\partial t}+u\frac{\partial \rho v}{\partial r}+v\frac{\partial \rho v}{\partial z}= -\frac{\partial P}{\partial r}+u\left(\frac{\partial^2 v}{\partial r^2}+\frac{\partial^2 v}{\partial z^2}+\frac{1}{r}\frac{\partial v}{\partial r}\right)+J_z\cdot B_\theta-F_v+\rho g \tag{3}$$

电流连续性方程

$$\frac{1}{r}\frac{\partial}{\partial r}\left(r\frac{\partial \varphi}{\partial r}\right)+\frac{\partial^2 \varphi}{\partial z^2}=0 \tag{4}$$

欧姆定律

$$J_r=-\frac{\partial \varphi}{\partial r} \tag{5}$$

$$J_z=-\sigma\frac{\partial \varphi}{\partial z} \tag{6}$$

安培定律

$$B_\theta=-\frac{u_0}{r}\int_0^r J_z r\mathrm{d}r \tag{7}$$

式中: u, v 分别表示径向速度和轴向速度; r 为径向坐标; g 为重力加速度; t 为时间; z 为轴向坐标; ρ为液体金属的密度; P 为压强; J_r 为半径方向电流密度; J_z 为轴向电流密度; μ为液态金属的动力粘度; σ为电导率; B_θ为自感应方向磁场; F_v 为拖拽力; φ为准电势; u_0为真空磁导率.

2.2　自由表面追踪 VOF 方法

为利用 VOF 方法追踪自由表面的轮廓, 引入一个单元体积分数的函数$F(i,j,t)$来追踪金属液滴

轮廓. $F(i,j,t)$满足下面的控制方程

$$\frac{\partial F}{\partial t}+\frac{\partial F}{\partial r}+\frac{\partial F}{\partial z}=0 \tag{8}$$

单元格状态如下

$$\begin{cases} F(i,j,t)=1 & \text{金属液体} \\ F(i,j,t)=0 & \text{离子气体} \\ 0<F(i,j,t)<1 & \text{金属液体与离子气体混合} \end{cases} \tag{9}$$

2.3 熔滴电流密度假定

根据文献 [12], 电流密度 J_z 在熔滴与焊丝的交界面处呈现均匀分布, 在熔滴端部呈现高斯分布, 即

$$J_z=\frac{kIh}{2\pi H}\cdot\exp\left(-kR^2\right)+\frac{I}{\pi r_s^2}\left(1-\frac{h}{H}\right) \tag{10}$$

$$k=\frac{1}{2\sigma_r^2} \tag{11}$$

式中: I 为焊接电流; H 为熔滴长度; h 为熔滴高度; r_s 为焊丝半径; R 为熔滴横截面半径; σ_r为高斯分布半径; k 为电流集中系数.

2.4 旋转电弧焊接热源半径

旋转电弧焊接过程中, 熔滴在电场力、磁场力及旋转离心力作用下, 形状难以确定. 根据能量守恒定律、送丝与熔化平衡关系及热源球形假设, 以单位时间内送丝量确定热源半径计算公式如下

$$V_Z=\pi {r_s}^2 v_s \tag{12}$$

$$\frac{4\pi {r_d}^3}{3}=\frac{V_Z}{4} \tag{13}$$

$$r_d=\sqrt[3]{\frac{3v_s r_s^2}{16}} \tag{14}$$

式中: V_Z 单位时间焊丝体积; v_s 送丝速度; r_d 热源半径.

3 模拟结果及分析

为分析旋转电弧焊接熔池成形过程中温度场与流场特性, 以能准确模拟含有自由表面流体流动功能的软件 Flow-3D 作为求解器, 计算域选用 0.4 mm 均匀矩形网格, 建立仿真模型, 然后对其进行成形过程模拟, 结果及分析如下.

3.1 旋转电弧堆焊熔池成形过程分析

旋转电弧熔池成形过程较为复杂, 主要从熔池成形时熔池内部区域温度变化以及液态金属对流特性来分析.

3.1.1 温度场分析

旋转电弧 GMAW 堆焊熔池模拟结果的温度场截面如图 2 所示.

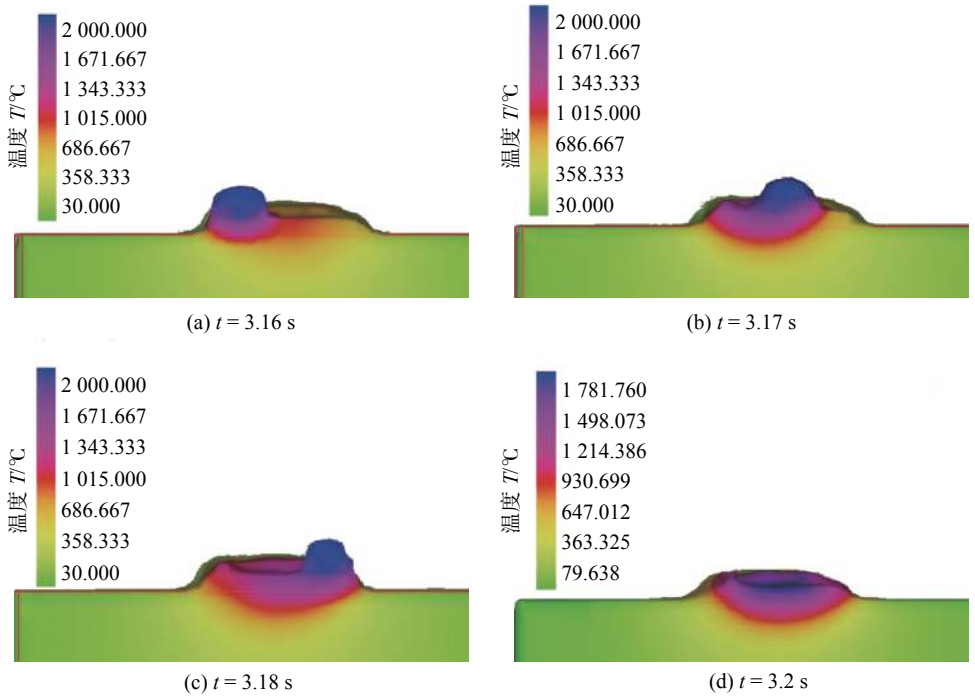

(a) t = 3.16 s (b) t = 3.17 s

(c) t = 3.18 s (d) t = 3.2 s

图 2 不同时刻熔池温度场分布

Fig. 2 Temperature field distribution of weld pool at different time. (a) t = 3.16 s; (b) t = 3.17 s; (c) t = 3.18 s; (d) t = 3.2 s

在 t = 3.16 s 时，熔滴进入熔池上端边缘处，逐渐熔化母材，使得局部熔池变深，热能向熔池中心扩散，集聚的热能加深熔池深度，并与上一熔滴的温度场连通，形成拖拽. 在 t = 3.17 s 时，熔滴进入熔池右端边缘处，逐渐熔化母材，使得局部熔池变深，热能向熔池中心扩散，集聚的热能加深熔池深度，并与上一熔滴的温度场连通，形成拖拽. 在 t = 3.18 s 时，熔滴进入熔池下端边缘处，逐渐熔化母材，使得局部熔池变深，热能向熔池中心扩散，集聚的热能加深熔池深度，并与上一熔滴的温度场连通，形成拖拽. 在 t = 3.2 s 时，熔池底部凝固，并逐渐完成成形过程.

3.1.2　流场分析

旋转电弧 GMAW 堆焊熔池模拟结果的流场截面如图 3 所示，熔滴接触熔池并向熔池过渡，由于焊丝旋转运动，导致熔滴下降时，作向外离心运动.

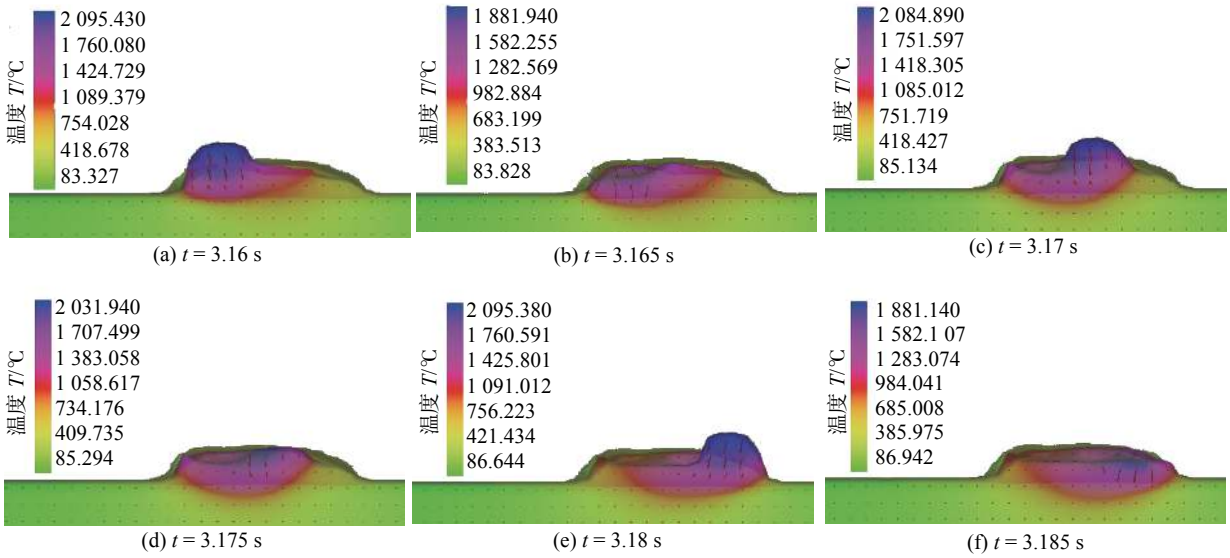

图 3　不同时刻熔池流场分布

Fig. 3　Velocity field distribution of weld pool at different time. (a) t = 3.16 s; (b) t = 3.165 s; (c) t = 3.17 s; (d) t = 3.175 s; (e) t = 3.18 s; (f) t = 3.185 s

在 t = 3.16 s 时，熔滴进入熔池上端边缘处，对应图 3a 所示位置，此时熔滴温度最高、熔滴内液态金属流动速度快，活跃液态金属由熔池最上侧向熔池中间流动. 在 t = 3.165 s 时，熔滴全部进入熔池，液态金属在熔池内，形成从边缘到中心处的回流，如图 3b 所示. 在 t = 3.17 s 时，熔滴进入熔池右端边缘处，对应图 3c 所示位置，其温度最高、熔滴内液态金属流动速度快，活跃液态金属由熔池最右侧向熔池中间流动. 在 t = 3.175 s 时，熔滴全部进入熔池，液态金属在熔池内，形成从边缘到中心处的回流，如图 3d 所示. 在 t = 3.18 s 时，熔滴进入熔池下端边缘处，对应图 3e 所示位置，此时熔滴温度最高、熔滴内液态金属流动速度快，活跃液态金属由熔池最下侧向熔池中间流动. 在 t = 3.185 s 时，熔滴全部进入熔池，液态金属在熔池内，形成从边缘到中心处的回流，形成完整对流过程，如图 3f 所示. 在拖拽的过程中液态金属由熔滴主体向熔池尾部流动. 熔滴旋转前进地向母材传导热能.

3.2　焊缝形成过程熔池分析

旋转电弧 GMAW 堆焊熔池成形过程的温度场如图 4 所示. 起弧时，熔池行为主要为旋转熔滴对母材的冲击，焊接进行一段时间之后，有一定的熔池积累，形成一段焊缝. 此时，熔滴过渡受到已冷却焊缝的阻碍以及焊缝尾部液态金属流动的影响.

在 t = 3.15 s 时，熔滴进入熔池最左端，热能向熔池中心扩散. 在 t = 3.16 s 时，熔滴进入熔池上端边缘处，热能向熔池中心扩散，与上一熔滴温度场相交，并形成拖拽. 在 t = 3.17 s 时，熔滴进入熔池最右端，热能向熔池中心扩散，与上一熔滴的温度场相交，并形成拖拽. 在 t = 3.18 s 时，熔滴进入熔池最下端边缘处，热能向熔池中心扩散，与上一熔滴的温度场相交，并形成拖拽. 一个周期内熔池内温度场成顺时针方向变化.

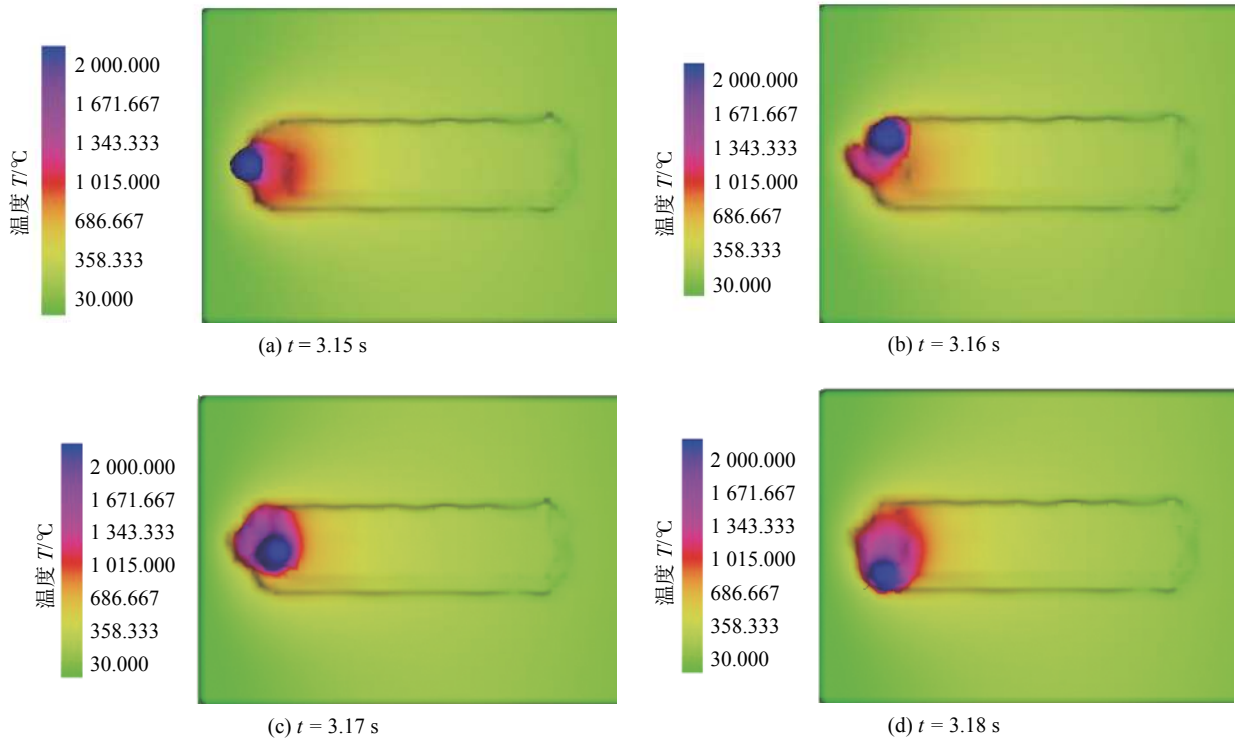

图 4 焊接过程温度场分布

Fig. 4 Temperature field distribation of welding process. (a) t = 3.15 s; (b) t = 3.16 s; (c) t = 3.17 s; (d) t = 3.18 s

4 试验与仿真结果对比分析

以表 1 参数进行旋转电弧 GMAW 堆焊试验，并将结果与仿真结果进行对比，以验证旋转电弧 GMAW 堆焊仿真结果.

试验装置如图 5 所示. 将试验焊缝切片后化学处理，得到所需要的截面，经测量得到：熔宽 9.06 mm，熔深 2.97 mm，模拟结果对应截面熔宽 8.76 mm，熔深 2.76 mm，如图 6所示.

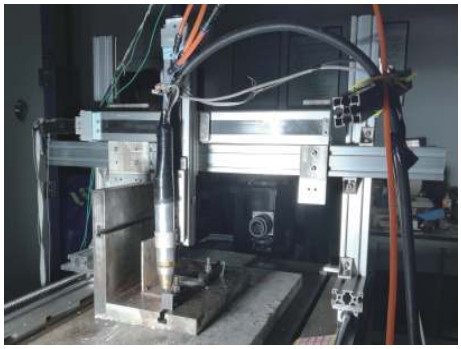

图 5 焊接试验装置

Fig. 5 Welding experiment device

试验熔池截面与仿真熔池截面对比，结果表明二者形状基本相同，熔宽与熔深参数接近，且实际熔池最大深度位于熔池中心与仿真的相应时刻熔

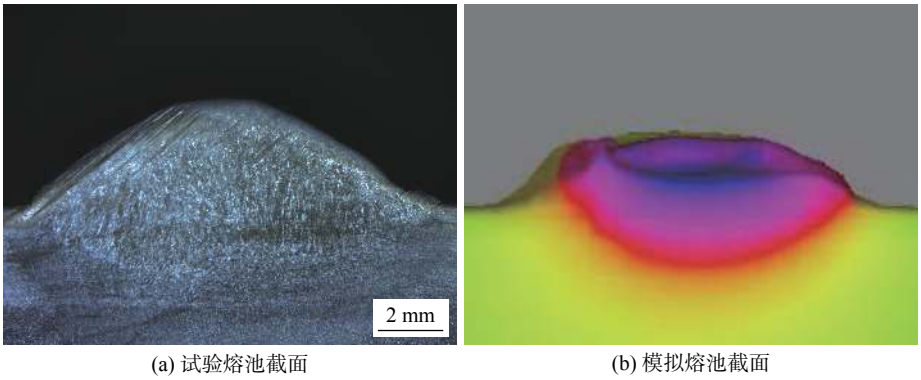

图 6 模拟与试验结果对比

Fig. 6 Comparison of simulation results with experimental results. (**a**) experimental weld pool section; (**b**) simulated weld pool section

池中心位置状态一致. 试验结果与模拟结果都存在明显的熔池底部形状不规则现象, 这是因为越靠近熔滴处, 熔池内部能量多, 母材熔化深度越大, 相比远离熔滴处的熔深要更大, 仿真截面局部的高温区域与试验截面中的最大熔深结果相对应.

5　结论

(1) 采用 Flow-3D 软件建立了旋转电弧堆焊短路过渡仿真模型, 基于 VOF 方法对熔池成形过程中熔池自由表面成形进行了追踪, 得到了旋转电弧 GMAW 堆焊成形过程.

(2) 熔池形成过程中, 熔池内同时存在因熔滴冲击力、电磁力引起的向内流动和因表面张力引起的向外流动. 旋转熔滴对熔池有搅拌作用, 流速变快, 并促使熔池内部液态金属体积变大, 熔池的宽度变大.

(3) 20 Hz 旋转频率下, 试验熔池截面形状与仿真熔池截面形状基本相同, 熔宽误差 0.3 mm, 熔深误差 0.2 mm, 且试验熔池最大深度位于熔池中心与仿真的相应时刻熔池中心位置状态一致.

参考文献

[1] Wu L, Cheon J, Kiran D V, *et al*. CFD simulations of GMA welding of horizontal fillet joints based on coordinate rotation of arc models[J]. Journal of Materials Processing Technology, 2016, 231(5): 221 − 238.

[2] Cho D W, Na S J. Molten pool behaviors for second pass V-groove GMAW[J]. International Journal of Heat and Mass Transfer, 2015, 88: 945 − 956.

[3] Wang Y, Tsai H L. Impingement of filler droplets and weld pool dynamics during gas metal arc welding process[J]. International Journal of Heat and Mass Transfer, 2001, 44(11): 2067 − 2080.

[4] Hozoorbakhsh A, Ismail M I S, Aziz N B A. A computational analysis of heat transfer and fluid flow in high-speed scanning of laser micro-welding[J]. International Communications in Heat and Mass Transfer, 2015, 68: 178 − 187.

[5] Wu D S, Hua X M, Ye D J, *et al*. Understanding of humping formation and suppression mechanisms using the numerical simulation[J]. International Journal of Heat and Mass Transfer, 2017, 104(1): 634 − 643.

[6] 吴东升, 华学明, 叶定剑, 等. MIG 焊接熔池形成与凝固过程数值模拟 [J]. 焊接, 2015(9): 6 − 11.
Wu Dongsheng, Hua Xueming, Ye Dingjian, *et al*. Numerical analysis of weld pool formation and solidification in MIG welding process[J]. Welding & Joining, 2015(9): 6 − 11.

[7] Cho D W, Kiran D V, Song W H, *et al*. Molten pool behavior in the tandem submerged arc welding process[J]. Journal of Materials Processing Technology, 2014, 214(11): 2233 − 2247.

[8] Tong L G, Gu J C, Yin S W, *et al*. Impacts of torch moving on phase change and fluid flow in weld pool of SMAW[J]. International Journal of Heat and Mass Transfer, 2016, 100: 949 − 957.

[9] Desmaison O, Bellet M, Guillemot G. A level set approach for the simulation of the multipass hybrid laser/GMA welding process[J]. Computational Materials Science, 2014, 91: 240 − 250.

[10] 张世亮, 胥国祥, 曹庆南, 等. 基于 FLUENT 软件的 GMAW 焊熔池动态行为数值分析模型 [J]. 焊接学报, 2018, 39(2): 75 − 79.
Zhang Shiliang, Xu Guoxiang, Cao Qingnan, *et al*. A numerical analysis model of weld pool dynamic behavior in GMAW based on FLUENT software[J]. Transactions of the China Welding Institution, 2018, 39(2): 75 − 79.

[11] Qiao L, Han T, Zhang H J, *et al*. Numerical study of fillet weld leg height of sleeve repair welding for in-service pipeline[J]. China Welding, 2018, 27(1): 32 − 40.

[12] 刘维球, 单彦广, 袁张. GMAW 焊接熔滴过渡过程的模拟研究 [J]. 热加工工艺, 2016, 45(21): 216 − 219.
Liu Weiqiu, Shan Yanguang, Yuan Zhang. Simulation of droplet transfer process in GMAW[J]. Hot Working Technology, 2016, 45(21): 216 − 219.

第一作者简介: 毛志伟, 1969 年出生, 博士, 副教授; 主要从事机器人与焊接自动化研究; 发表论文 30 多篇; Email: ndmao@163.com.

（编辑:　钟常远）

location methods, under certain welding conditions, finally, identifiing the detection signal by statistical probability feature recognition, which realized the abstract separation of welding penetration feature information. And the method has obtained the reliable penetration detection results.

Key words: laser welding; penetration detection; mesoscopic extraction; statistical analysis

Effect of banded structure on mechanical properties of aluminum/magnesium dissimilar metal friction stir welding joint ZHU Hao[1], ZHANG Erlong[1], MO Shuxian[1], MA Zeming[1], WANG Jun[2] (1. Shijiazhuang TIEDAO University, Shijiazhuang, 050043, China; 2. Hebei University of Science and Technology, Shijiazhuang, 050018, China). pp 34-38,66

Abstract: The flat butt welding tests of different processes for 6061 aluminum alloy and AZ31B magnesium alloy with thickness of 4 mm were carried out by friction stir welding (FSW). Microstructure of the joints was observed and analyzed by optical microscopy (OM), scanning electron microscopy (SEM), X-ray diffraction (XRD) and energy dispersive spectrometer (EDS), mechanical properties of the joints were tested by electronic universal testing machine. The results show that, there are obvious banded structures in the weld nugget zone (WNZ), which are composed of aluminum slices inserted in the magnesium matrix and IMCs dispersed on the band. The types of IMCs are $Al_{12}Mg_{17}$ and Al_3Mg_2. Crack nucleation and propagation of aluminum/magnesium dissimilar metal FSW joints occur among the banded structure. Welding technology affects the morphology of banded structure and size and quantity of IMCs. With the increasing of rotational speed (n) or the decreasing of welding speed (v), the banded structure in the joint WNZ are curved, relatively short in length and discontinuously distributed. The banded structure becomes thinner, but the quantity of IMCs increase and the size becomes larger when the rotation speed (n) is too high or the welding speed (v) is too low. The ultimate strength of aluminum/magnesium dissimilar metal FSW joint mainly depends on the morphology of the banded structure and the size and quantity of IMCs.

Key words: aluminum/magnesium dissimilar alloy; friction stir welding; banded structure; mechanical properties

Effect of normalizing temperature on microstructure and properties of Ti-6Al-4V fabricated by arc additive manufacturing XU Guojian, LIU Jin, CHEN Dongsa, MA Ruixin, SU Yunhai (Shenyang University of Technology, Shenyang, 110870, China). pp 39-43

Abstract: The samples of TC4 titanium alloy were prepared by TIG arc additive manufacturing, and the samples were normalized. The results show that the microstructure of the sample is composed of α phase and β phase after normalizing treatment. And the acicular primary α phase becomes shorter and thicker with the increase of normalizing temperature at the range of 750 ~ 950 °C, and gradually changes to the direction of net basket structure. At the range of 950 ~ 1 050 °C, some primary α phases develop toward "pseudo-equiaxed crystals", and form structures which comprises the "pseudo-equiaxed crystals" primary α phase + the fine needle-like primary α phase + (α + β) structures between the fine needle-like primary α phases at 1 050 °C. The better mechanical properties of the present work (in conditions of 850 °C/2 h/AC) show that tensile strength, yield strength, elongation and reduction of the area in y direction are 900.4, 820.4 MPa, 9.3%, and 27.4% respectively, and tensile strength, yield strength, elongation and reduction of the area in z direction are 890.1, 790.1 MPa, 10.8%, and 31.0% respectively, which is close to the standard requirements for forgings. The hardness of sedimentary state and normalizing state has little changes. The fracture morphology of tensile specimen (z tensile specimen and y tensile specimen) is full of dimples and belongs to plastic fracture.

Key words: TC4 (Ti-6Al-4V); normalizing treatment; TIG arc additive manufacturing (TIG AAM); microstructure; mechanical properties

Dynamic simulation of GMAW short circuiting transfer pool in rotating arc surfacing MAO Zhiwei[1], HUANG Tao[1], ZHOU Shaoling[2] (1. Nanchang University, Nanchang, 330031, China; 2. Jiangxi Industry Polytechnic College, Nanchang, 330095, China). pp 44-49

Abstract: In order to explore the forming temperature and convective distribution law of the gas metal arc welding (GMAW) short circuiting transfer pool formed by rotary arc surfacing, a three-dimensional mathematical model was established by using Flow-3D software, and a spherical rotaing heat source model was used to simulate the molten pool forming law during the short-circuit transition of the rotating arc in GMAW with workpiece material Q235, considering the gravity, drag force, surface tension and buoyancy. The volume of fluid (VOF) method is used to trace the droplet transition and the free deformation of the pool surface, and the changes of temperature field and flow field inside the molten pool when the droplet enters the pool was analyzed. The results show that during the formation of the molten pool, the rotating droplet has a stirring effect on the molten pool, and makes the liquid metal in the molten pool more active, the flow rate faster, the volume of the liquid metal in the molten pool becomes larger, and the width of the molten pool becomes larger. The simulated weld size and shape are in good agreement with the test, which provide a reference for optimizing the welding process parameters to improve the quality of the rotaryarc

GMAW surfacing weld.

Key words: rotating arc welding; spherical rotating heat source model; melt pool flow; melt pool solidification

Effect of Nd addition on microstructure and mechanical properties of Sn-0.7Cu-0.05Ni soldered joints LIU Shuang, XUE Songbai (Nanjing University of Aeronautics and Astronautics, Nanjing, 210016, China). pp 50-54

Abstract: The effects of Nd addition on the microstructure and mechanical properties of Sn-0.7Cu-0.05Ni/Cu soldered joints under as-reflowed and 150 °C isothermal-aging process were investigated. The results indicated that an appropriate amount of Nd addition could obviously improve the interfacial microstructure and the mechanical properties of Sn-0.7Cu-0.05Ni soldered joints. The optimum properties were obtained while Nd addition was 0.06wt. %. Besides, the growth of the Sn-Cu-Ni/Cu intermetallic compound layer under aging process was restrained by adding 0.06wt.% Nd, which would enhance the reliability of the soldered joints during service process. After aging for 1 440 h, the shear force of Sn-0.7Cu-0.05Ni-0.06Nd soldered joints still ranked the best among all of the tested solders, increased by 31.9% compared to the Nd-free Sn-Cu-Ni soldered joints.

Key words: Nd; Sn-Cu-Ni solders; microstructure; mechanical properties

Effect of Si content in welding wire on crack sensitivity of aluminum alloy joints and its mechanism WANG Jun, LI Fang, ZHANG Yuelong, HUA Xueming, SHEN Chen (Shanghai Key Laboratory of Laser Manufacturing and Material Modification, Shanghai Jiaotong University, Shanghai, 200240, China). pp 55-60

Abstract: Using scanning electron microscopy, energy spectrum, and real-time acquisition of temperature fields, the effects and mechanisms of Si content in the welding wire on the sensitivity to thermal cracking of AA6063 aluminum alloy GMAW welded joints were studied. The results show that when the welding wire is pure aluminum, slender welding cracks appear in the center of the weld of the fishbone sample; when the Si content in the welding wire is 4.5% ~ 6%, the length of the crack is short, but the cracking distance is obviously increased; when the Si content in the welding wire reached 11% ~ 13%, no cracks appeared in the sample weld. With the continuous increase of Si content, the solidification temperature range of alloy prone to crack increases first and then decreases. The difference of Si content in welding wire will also affect the fluidity of molten metal at the later solidification stage, making the phase composition and morphology at the grain boundary of weld obviously different. At the same time, the increase of Si content will make the cooling rate of the joint increase first and then decrease, thus causing the stress state to change, and the thermal crack sensitivity increases first and then decreases.

Key words: Si content; aluminum alloy; GMAW welding; crack sensitivity

Rapid fatigue strength assessment of SUS301L-Q235B dissimilar materials spot-welded joint based on infrared thermography SUN Yang[1,2], LIU Yaliang[1,2], LI He[1,2], YANG Xinhua[1,2], XU Hongji[1,2] (1. Dalian Jiaotong University, Dalian, 116028, China; 2. Liaoning Key Laboratory of Welding and Reliability of Rail Transportation Equipment, Dalian, 116028, China). pp 61-66

Abstract: In this paper, with the help of high performance infrared thermal imager, local hot spots of nugget and plastic ring on the side of SUS301L stainless steel of the SUS301L-Q235B dissimilar materials spot-welded joint was monitored. And the quantitative relationship between the temperature rise slope and the fatigue limit of the welding joint of dissimilar materials was established. Then, a method to predict the fatigue limit of the spot-welded joint of dissimilar materials based on the tipping point of temperature rise. The results show that a serious nugget migration generates on the Q235B side of SUS301L-Q235B dissimilar materials spot-welded joint, which results in reduction of the carrying capacity of stainless steel. Under the action of high frequency shear tensile, the "four stages" temperature evolution characteristics are presented. The fatigue limit predicted by infrared thermography was 5.569 kN. The fatigue limit obtained by the traditional staircase method was 5.875 kN. The error between the predicted value and the test value was 5.21%, which presents a high concordance. The rapid fatigue limit prediction proposed in this paper can overcome the limitations of the traditional fatigue test method and realize non-contact and non-destructive prediction of spot-welded joint fatigue limit of dissimilar materials, which has important engineering significance and research value.

Key words: infrared thermography; dissimilar materials; fatigue strength; rapid assessment; spot welding

First principle calculation of the binding mechanism between Ti and SiO_2 XUE Haitao, WEI Xin, GUO Weibing, ZHANG Xiaoming (Hebei University of technology, Tianjin, 300130, China). pp 67-71

Abstract: Ti is an important active element to join SiO_{2f}/SiO_2 composite materials. Therefore, the bonding mechanism of Ti and SiO_2 was studied by using first principle calculation. Two kinds of interfaces with different termination and stoichiometric ratio were studied by the results of work of separation (W_{sep}), electron behavior and interface energy. It is found that in the O-terminated interface, Ti and O atoms form a